High-fidelity Raman matterwave control by composite biased rotations

Liyang Qiu,[1,*] Haidong Yuan,[2] and Saijun Wu[1]

[1]*Department of Physics, State Key Laboratory of Surface Physics and Key Laboratory of Micro and Nano Photonic Structures (Ministry of Education), Fudan University, Shanghai 200433, China*

[2]*Department of Mechanical and Automation Engineering, The Chinese University of Hong Kong, Shatin, Hong Kong, China*

(Received 13 June 2023; accepted 25 August 2023; published 27 October 2023)

Precise control of hyperfine matterwaves via Raman excitations is instrumental to a class of atom-based quantum technology. We investigate the Raman matterwave control technique for alkaline-like atoms in an intermediate regime characterized by the single-photon detuning where a choice can be made to balance the Raman excitation power efficiency with the control speed, excited-state adiabatic elimination, and spontaneous-emission suppression requirements. Within the regime, rotations of atomic spinors by the Raman coupling are biased by substantial light shifts. Taking advantage of the fixed bias angle, we show that composite biased rotations can be optimized to enable precise ensemble spinor matterwave control within nanoseconds, even for multiple Zeeman pseudospins defined on the hyperfine ground states and when the laser illumination is strongly inhomogeneous. Our scheme fills a technical gap in light pulse atom interferometry for achieving high-speed Raman spinor matterwave control with moderate laser power.

DOI: 10.1103/PhysRevResearch.5.043094

I. INTRODUCTION

From inertial and gravity sensing [1–4] to quantum simulation [5,6] and computation [7–12], atom interferometric sensing of spin- and spatial-dependent interaction is highly useful for atom-based quantum technology. Operating the interferometry technique in the quantum regime [13–16] requires high-fidelity coherent control of spinor matterwaves. However, for generic reasons associated with phase-space density limitations, atomic wave function, and ballistic expansion, as well as the imperfect optical field collimation itself, a free-space matterwave can hardly be sufficiently localized in space to be immune to inhomogeneous optical field broadening. To this end, the composite pulse (CP) technique originally developed in nuclear magnetic resonance (NMR) [17–21] becomes particularly useful for realizing error-resilient "spinor matterwave gates" with light in order to achieve ultrahigh-control fidelity. However, a prerequisite for achieving the goal is to rapidly manipulate the isolated pseudospins defined on pairs of atomic levels before any decoherence occurs, and even before the atoms move.

Pioneering efforts toward precise control of two-level atomic "spinor" matterwaves based on two-photon Raman excitations were made during the development of light pulse atom interferometry [22–25] and ion-based quantum information processing [9,26]. As in Fig. 1(a), here the atomic pseudospin is defined on a pair of ground-state hyperfine levels split by $\omega_{\rm HF}$ in frequency, referred to as $|\downarrow\rangle$, $|\uparrow\rangle$. The $\mathbf{k}_{1,2}$ optical pulses with duration τ_c, Rabi frequencies $\Omega_{1,2}$, and optical frequency difference $\omega_1-\omega_2=\omega_{\rm HF}$ resonantly drive the spin-flip while transferring the $\hbar\mathbf{k}_{\rm R}$ photon momentum to the spinor matterwave ($\mathbf{k}_{\rm R}=\mathbf{k}_1-\mathbf{k}_2$). For short enough τ_c so that the atomic motion is negligible, the spinor matterwave can be uniformly controlled by a Raman coupling $\Omega_{\rm R}$ on the Bloch sphere [Fig. 1(c)] for realizing, e.g., matterwave splitters and mirrors [27]. To perfect the Raman matterwave controls, the two-level atomic spinors need to be isolated from multilevel excitations and spontaneous emission. To manipulate macroscopic samples, the control needs to be designed in a manner insensitive to the laser intensity inhomogeneity [24,25,28–30]. To this end, an important parameter for the Raman control is the single-photon detuning Δ. To ensure a laser-intensity-independent two-photon detuning δ, highly important for precision measurements, a moderate single-photon detuning $\Delta<\omega_{\rm HF}$ is typically chosen to nullify the differential Stark shift [31]. But this choice of Δ fundamentally limits the control fidelity associated with spontaneous emission. Furthermore, associated with the excited-state-elimination requirements [32], the moderate Δ also limits the available Raman control speed for mitigating low-frequency noises, including those due to the atomic motion [30,33,34]. Separately, for Raman control of microscopically confined ions, a THz-level Δ comparable to the fine-structure splitting $\omega_{\rm F}$ can be chosen to minimize the Stark shifts [35]. However, since $\Omega_{\rm R}\propto 1/\Delta$, the technique can hardly be applied to macroscopic samples without either substantially sacrificing the operation speed or requiring enormous laser power.

In this work, we report the systematic development of a method to construct fast Raman control of spinor

*Present address: Max-Planck-Institut für Quantenoptik, 85748 Garching, Germany; liyang.qiu@mpq.mpg.de

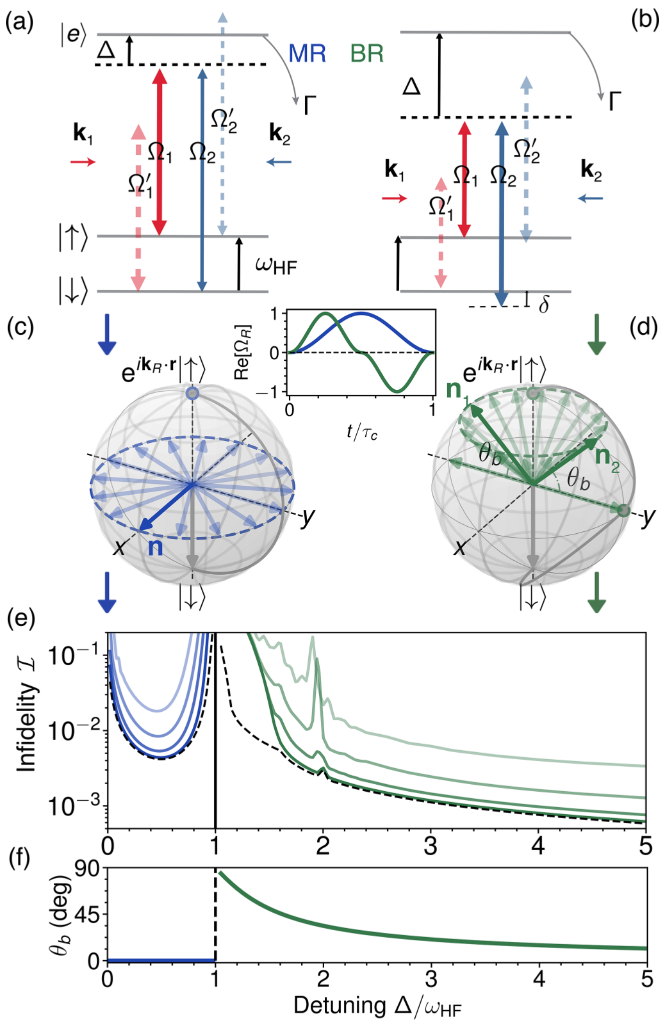

FIG. 1. Comparison between the resonant Raman controls in the MR (a),(c) and BR (b),(d) regime. (a),(b) The level diagrams. (c),(d) Bloch sphere representation of the optical Raman control under the two-level approximation. The radial array of light arrows denotes available rotation axes $\mathbf{n}$ for the generalized Raman Rabi vectors $\vec{\boldsymbol{\Omega}}_{\mathrm{R}} = (\Omega_{\mathrm{R}}\cos\varphi, \Omega_{\mathrm{R}}\sin\varphi, \delta)$. For (c) with $\delta = 0$ (MR, with I_1/I_2 adjusted according to Ref. [31]), the axes are on the equator. For (d) the axes are biased by $\theta_b = \tan^{-1}(\delta/|\Omega_{\mathrm{R}}|)$ (BR, with the I_1/I_2 ratio set as unity here). Gray curved lines represent typical spin trajectories during a π rotation in the two cases. (e) Minimal gate infidelities $\mathcal{I}$ for the rotation $R_x(\pi)$ vs Δ with numerical simulation on the ^{87}Rb D1 line (Appendix A, with $\omega_{\mathrm{hfs},e} = 0$). Four lines in blue (MR) and green (BR) from light to deep represent minimal achievable errors at $\omega_{\mathrm{HF}}\tau_c/\pi = 20, 50, 100, 200$, respectively. The dashed line denotes the long-time limit, which is evaluated by increasing τ_c to $1000\pi/\omega_{\mathrm{HF}}$. The features near $\Delta/\omega_{\mathrm{HF}} = 2$ are due to multiphoton resonances. Notice here that the simple $N = 2$ double pulse scheme requires $\theta_b < 45^\circ$, corresponding to $\Delta/\omega_{\mathrm{HF}} > 1.618$ for $I_1/I_2 = 1$ (Appendix C). Part (f) gives the bias angle θ_b in the (e) simulation.

matterwaves in an unconventional regime of single-photon detuning Δ. Our work is motivated by the observation that between the conventional choices of Δ for light pulse atom interferometry and trapped-ion quantum information processing, $\omega_{\mathrm{HF}} < \Delta \ll \omega_{\mathrm{F}}$, the typically unfavored nonzero Stark shift to the two-photon detuning δ is proportional to the Raman Rabi frequency Ω_{R}. The Raman controls are therefore rotations of atomic spins on the Bloch sphere with the axes biased by a fixed angle θ_b from the equator [Fig. 1(d)]. The proportionality ensures simple composite strategies [36–38] for driving universal qubit gates for the spinor matterwave within nanoseconds where atomic motional effects including the two-photon Doppler shifts become negligible [28,29,33]. Furthermore, since within this biased rotation (BR) regime the errors in the detuning δ and intensity I are perfectly correlated, a simple SU(2) optimization strategy can be applied to achieve precise ensemble control [18,19] of large alkali samples, even with a focused, nonuniform laser beam. Unbounded by traditional choices of single-photon detuning Δ [31,35], our scheme conveniently supports the adjustable balance of Raman excitation optical power efficiency with the requirements of the control speed and/or the suppression of excited-state dynamics for coherently transferring a large amount of photon recoil momenta to specific samples in a spin-dependent manner [5,6,22,39], and for achieving precise spinor matterwave control in quantum-enhanced atom interferometric applications [13–16].

II. BIASED ROTATION

We consider the Fig. 1(a) Raman configuration. The traveling pulses with electric field envelopes $\mathcal{E}_{1,2}e^{i(\mathbf{k}_{1,2}\cdot\mathbf{r}+\phi_{1,2})}$ and duration τ_c drive the $|\uparrow\rangle - |e\rangle$ and $|\downarrow\rangle - |e\rangle$ Rabi couplings $\Omega_{1,2}$ (solid double arrows), as well as the $\Omega'_{1,2}$ (dashed double arrows) with the ground states interchanged. With a large single-photon detuning $\Delta \gg 1/\tau_c$, the excited levels $|e\rangle$ can be adiabatically eliminated from the ground-state dynamics [32]. While both $\Omega_{1,2}$, $\Omega'_{1,2}$ are proportional to $\mathcal{E}_{1,2}$, efficient $|\downarrow\rangle \leftrightarrow |\uparrow\rangle$ Raman matterwave coupling can only be induced by $\Omega_{1,2}$ when $\omega_{\mathrm{HF}} \gg 1/\tau_c$, since the counter-rotating Raman transitions induced by $\Omega'_{1,2}$ are energetically suppressed by the hyperfine splitting. An effective Hamiltonian to describe the ground-state spinor can be written as

$$H = -\tfrac{1}{2}\hbar\delta\sigma_z + \tfrac{1}{2}\hbar|\Omega_{\mathrm{R}}|(\sigma_x\cos\varphi + \sigma_y\sin\varphi). \tag{1}$$

Here $\sigma_{x,y,z}$ are Pauli matrices. The Raman Rabi coupling $\Omega_{\mathrm{R}} = \Omega_1^*\Omega_2/2\Delta$, with phase $\varphi = \phi_2 - \phi_1$, can be designed by shaping the pulse envelopes $\mathcal{E}_{1,2}$. The $\delta = \delta_\uparrow - \delta_\downarrow$ in Eq. (1) is the two-photon detuning by the Stark shifts,

$$\delta = \frac{|\Omega_1|^2}{4\Delta} + \frac{|\Omega'_2|^2}{4(\Delta - \omega_{\mathrm{HF}})} - \frac{|\Omega_2|^2}{4\Delta} - \frac{|\Omega'_1|^2}{4(\Delta + \omega_{\mathrm{HF}})}. \tag{2}$$

For short enough τ_c [40] and with spatially uniform intensities $I_{1,2} = |\mathcal{E}_{1,2}|^2$ [41], the delocalized spinor matterwave $|\psi(\mathbf{r})\rangle = \psi_\downarrow(\mathbf{r})|\downarrow\rangle + \psi_\uparrow(\mathbf{r})e^{i\mathbf{k}_{\mathrm{R}}\cdot\mathbf{r}}|\uparrow\rangle$ can be uniformly controlled with a single set of $(\delta, \Omega_{\mathrm{R}})$ parameters by Eq. (1). Practically, to achieve ultraprecise matterwave control with a precision similar to that for internal spins [42–44], particularly for large samples with inhomogeneous $I_{1,2}$ [see Fig. 2(a), inset], the spinor matterwave control must be achieved in an intensity-insensitive manner. In particular, the dependence of δ on $I_{1,2}$ can be suppressed at moderate $\Delta < \omega_{\mathrm{HF}}$, which we refer to as a "magic ratio" (MR) regime [Figs. 1(a) and 1(c)], by tuning the I_1/I_2 ratio [31].

In this work, instead of minimizing the dependence of δ on $I_{1,2}$ [26,31,35], we focus on Raman spinor matterwave control

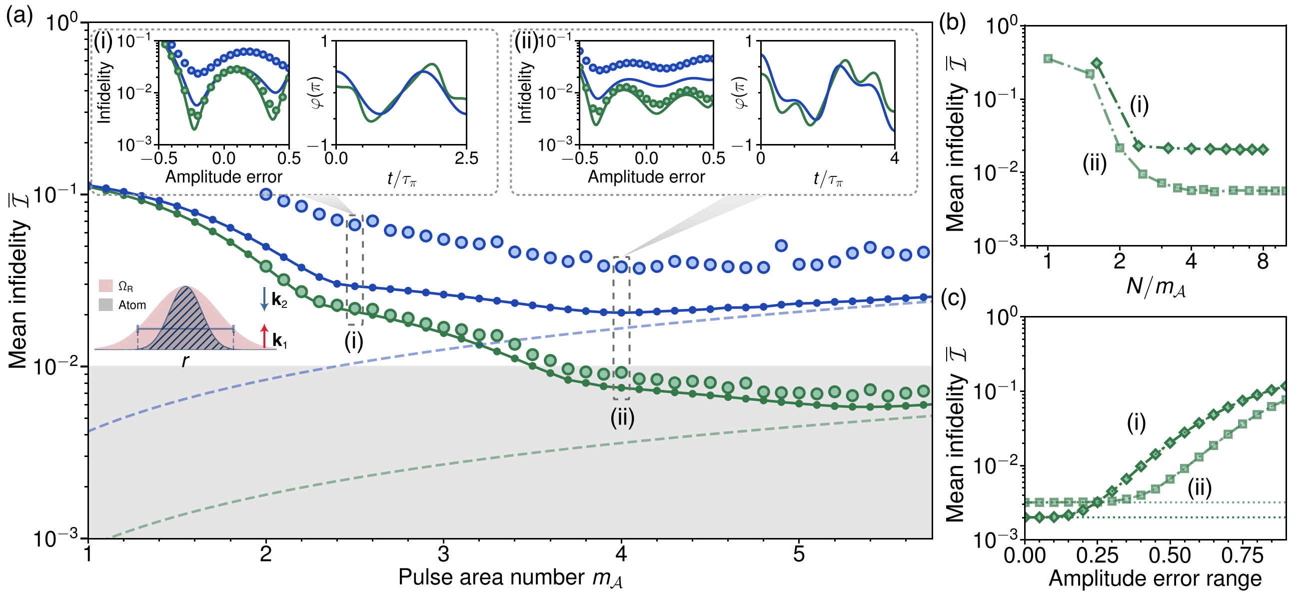

FIG. 2. (a) Performance of an $R_x(\pi)$ gate with CP-BR ($b = 0.3$, $\Delta = 3.6\omega_{\rm HF}$, green) and CP-MR ($b = 0.0$, $\Delta = 0.5\omega_{\rm HF}$, blue). The infidelity $\overline{\mathcal{I}}$ averaged over $\varepsilon_{\mathcal{A}}/\mathcal{A} = \pm 50\%$ is plotted vs $m_{\mathcal{A}}$. The dashed lines give the Eq. (5) spontaneous-emission limit. The solid lines with points give $\overline{\mathcal{I}}$ according to SU(2) calculations superimposed on the spontaneous-emission loss. The circle symbols give $\overline{\mathcal{I}}$ according to full-level ^{87}Rb D-line simulation, with the SU(2)-optimized $\{\varphi_j\}_{\rm opt}$ and edge-smoothed $|\Omega_{\rm R}(t)|$, $\tau_c = (m_{\mathcal{A}} + \pi/2 - 1)\tau_\pi$, with $\tau_\pi = 100/\omega_{\rm HF} = 7.4$ ns. The top insets give typical $\mathcal{I}$ vs $\varepsilon_{\mathcal{A}}/\mathcal{A}$, before the ensemble average, by the optimal pulse with a phase profile $\{\varphi_j\}_{\rm opt}$ [before the $|\Omega_{\rm R}(t)|$ edge-smoothing], with $m_{\mathcal{A}} = 2.5$ (i) and $m_{\mathcal{A}} = 4$ (ii). The solid lines and circle symbols correspond are from two-level and full-level simulations, respectively. (b) $\overline{\mathcal{I}}$ vs subpulse number N, evaluated with the two-level model, with other parameters by (a,i) and (a,ii). (c) $\overline{\mathcal{I}}$ vs amplitude error range $\varepsilon_{\rm M}$, evaluated with the two-level model, with other parameters by (a,i) and (a,ii) denoted by small diamond and square symbols, respectively. The lower and upper dotted lines denote the spontaneous-emission limit of (i) and (ii), respectively. Here, during both optimization and evaluation, amplitude deviation uniformly samples $\varepsilon_{\mathcal{A}} \in (-\varepsilon_{\rm M}, \varepsilon_{\rm M})\mathcal{A}$ for each data point.

within $\omega_{\rm HF} < \Delta \ll \omega_{\rm F}$ so the two-photon shift δ is substantial. Correspondingly, the spin rotation axes as in Fig. 1(d) are biased from the equator of the Bloch sphere by

$$\theta_b = \tan^{-1}(\delta/|\Omega_{\rm R}|). \tag{3}$$

Although the θ_b-bias appears inconvenient, for matterwave Raman control with uniform $I_{1,2}$, the bias is easily compensated for by simple composite pulses [36–38]. The simplest idea of double-pulse [36] BR is illustrated in Fig. 1(d). Here, as long as $\theta_b < \pi/4$, then a double-pulse Raman control can be synthesized for $R_x(\pi)$, a π-rotation of spin along the x-axis. The first subpulse with Raman "Rabi vector" $\vec{\Omega}_{\rm R} = (|\Omega_{\rm R}|\cos\varphi, |\Omega_{\rm R}|\sin\varphi, \delta)$ transports the state vector to the equator during $0 < t < \tau_c/2$. The second subpulse, with $\varphi \to \varphi + \pi$ realized by introducing a relative π phase-jump between $\mathcal{E}_{1,2}$ [Fig. 1(b)], completes the spin inversion during $\tau_c/2 < t < \tau_c$.

To illustrate the BR advantages in real atoms, in Fig. 1(e) we compare the performance of the exemplary $R_x(\pi)$ rotation ($U = -i\sigma_x$) on the ^{87}Rb D1 line (Fig. 4) [45] in the MR regime ($\Delta < \omega_{\rm HF}$, with suitable I_1/I_2 to nullify δ [31]) with those achievable in the BR regime ($\Delta > \omega_{\rm HF}$ with a fixed $I_1/I_2 = 1$). The gate fidelity is defined as

$$\mathcal{F} = \frac{1}{6}\sum_{j=1}^{6} |\langle\psi_j|U^\dagger\tilde{U}|\psi_j\rangle|^2. \tag{4}$$

Here U is the target operator in the $\{|\uparrow\rangle, |\downarrow\rangle\} = \{|\uparrow_0\rangle, |\downarrow_0\rangle\}$ spin-space, defined on the ^{87}Rb $5S_{1/2}$ clock transition (Fig. 4) for now. The $\tilde{U} = \hat{P}_\sigma \hat{T} e^{-i/\hbar\int_0^{\tau_c} H_{\rm eff}dt}\hat{P}_\sigma$ is the actual D1 evolution operator projected to the spin space ($\hat{P}_\sigma$ is the projection operator), evaluated by integrating the Schrödinger equation with the non-Hermitian Hamiltonian $H_{\rm eff} = H_0 - i\frac{\hat{\Gamma}}{2}$. The H_0 describes the full vectorial laser-atom interaction, while $\hat{\Gamma}$ describes the spontaneous emission from $|e\rangle$, detailed in Appendix A. The gate fidelity is obtained by averaging a set of $\{|\psi_j\rangle, j = 1, \ldots, 6\}$ initial states, which are the three pairs of eigenstates for $\sigma_{x,y,z}$ [46]. A large $\mathcal{F}$ ensures high-quality SU(2) rotation independent of the initial atomic states, which is key to performing coherent spinor matterwave control.

We emphasize that the Eq. (1) Hamiltonian is obtained by adiabatically eliminating excited levels $|e\rangle$ [32] and ignoring the counter-rotating $\Omega'_{1,2}$ Raman terms, both requiring the optical fields to vary as slowly as possible. To maintain the associated approximations, the optical pulses with duration τ_c are "sine-shaped" (Appendix A) to minimize the impact of nonadiabatic $|e\rangle$ excitations and counter-rotating couplings. To simplify the analysis, in the Fig. 1(e) example only, the excited-state hyperfine splitting $\omega_{{\rm hfs},e}$ is set to zero to fully suppress the leakages of atomic population among the Zeeman sublevels for the linearly polarized pulses [30,47] (Appendix A). The infidelity $\mathcal{I} = 1 - \mathcal{F}$ degrades at short τ_c, since the shorter τ_c is associated with a stronger spectra component to excite $|e\rangle$. By increasing τ_c to $100\pi/\omega_{\rm HF}$ and for, e.g., $\Delta > 2.5\omega_{\rm HF}$, nonadiabatic excitations to $|e\rangle$, including those associated with multiphoton resonances, are effectively suppressed. In this $|e\rangle$-elimination limit where the hyperfine rotating-wave approximation is also well-satisfied, the gate dynamics follows the Eq. (1) SU(2) model [Figs. 1(c) and 1(d)] with the infidelity $\mathcal{I}$ reaching a minimal spontaneous-emission error $\mathcal{I}_{\rm sp}$ associated with the dressed ground states,

$$\mathcal{I}_{\rm sp} = \eta\mathcal{A}\Gamma/\Delta. \tag{5}$$

Here $\mathcal{A} = \int_0^{\tau_c} |\Omega_{\rm R}|d\tau$ is the Raman pulse area for completing $R_x(\pi)$. The factor η of order unity depends on the detuning Δ and the choice of I_1/I_2 ratio. For example, in Fig. 1(e) this spontaneous-emission limit is given by the dashed lines (except the $1 < \Delta/\omega_{\rm HF} < 1.618$ interval where the simple two-pulse BR fails at $I_1/I_2 = 1$). For this fictitious ^{87}Rb example, the Fig. 1(e) results clearly demonstrate the BR advantages, with $\mathcal{F} > 99.8\%$ achievable at $\tau_c = 100\pi/\omega_{\rm HF}$ and $\Delta > 2.5\omega_{\rm HF}$, which cannot be reached in the traditional MR regime even in the long-τ_c limit. We note that this BR-to-MR advantage is more pronounced with increased $\Gamma/\omega_{\rm HF}$ ratio in lighter alkalis, and when $\omega_{{\rm hfs},e}$ is included, as will be discussed with Fig. 2 on more sophisticated CP with intensity-error resilience.

III. COMPOSITE-BR WITH DESIGNED ROBUSTNESS

Practically, as illustrated in the inset of Fig. 2(a), the optical Raman control of large samples is prone to $\Omega_{\rm R} \propto \sqrt{I_1 I_2}$ amplitude errors associated with intensity inhomogeneity. For the pulsed controls, the amplitude error is characterized by a distribution of deviation $\{\varepsilon_\mathcal{A}\}$ from the designed Raman pulse area $\mathcal{A}$. Separately, the two-photon detuning δ in Eq. (1) can also be broadened [31], such as by the two-photon Doppler shift if the atomic sample has substantial velocity distribution along $\mathbf{k}_{\rm R}$ [29,34,48]. The common resolution to suppressing the errors associated with the $(\varepsilon_\mathcal{A}, \varepsilon_\delta)$ deviations relies on ensemble optimal control techniques [18,19], which can be implemented with composite pulses [17,20,29,48].

Here, with $\tau_c \sim 100\pi/\omega_{\rm HF}$ within tens of nanoseconds for typical alkalis, the errors induced by the two-photon Doppler shifts (denoted as $\delta_{\rm off}$, to be discussed later) are typically negligible in cold atomic samples [24,25,30] and collimated atomic beams [22]. The Stark-shifted $\delta = b|\Omega_{\rm R}|$ is proportional to $|\Omega_{\rm R}|$ with the bias ratio $b = \tan\theta_b$. At a fixed I_1/I_2 and for a fixed pair of atomic levels to form the $\{|\uparrow\rangle, |\downarrow\rangle\}$ pseudospin [Figs. 4 and 3(a)], then the ε_δ and $\varepsilon_\mathcal{A}$ errors are perfectly correlated to support a simpler CP-BR strategy. To optimize the robustness of CP-BR, we split an $\mathcal{A}$-area Raman pulse into N equiangular subpulses [21] with Raman phases φ_j. The full evolution operator

$$\tilde{U}^{(N)}(\mathcal{A}, b; \{\varphi_j\}) = \prod_j^N \tilde{U}(\mathcal{A}/N, b; \varphi_j) \tag{6}$$

becomes a product (multiply from left) of the single-pulse propagators $\tilde{U}_j = \tilde{U}(\mathcal{A}/N, b; \varphi_j)$. We then optimize the fidelity averaged over the list of $\{\varepsilon_\mathcal{A}\}$ deviation of interest for realizing a certain operation U,

$$\overline{\mathcal{F}}(\mathcal{A}, b; \{\varphi_j\}) = \langle \mathcal{F}^{(N)}(\mathcal{A} + \varepsilon_\mathcal{A}, b; \{\varphi_j\})\rangle_{\{\varepsilon_\mathcal{A}\}}. \tag{7}$$

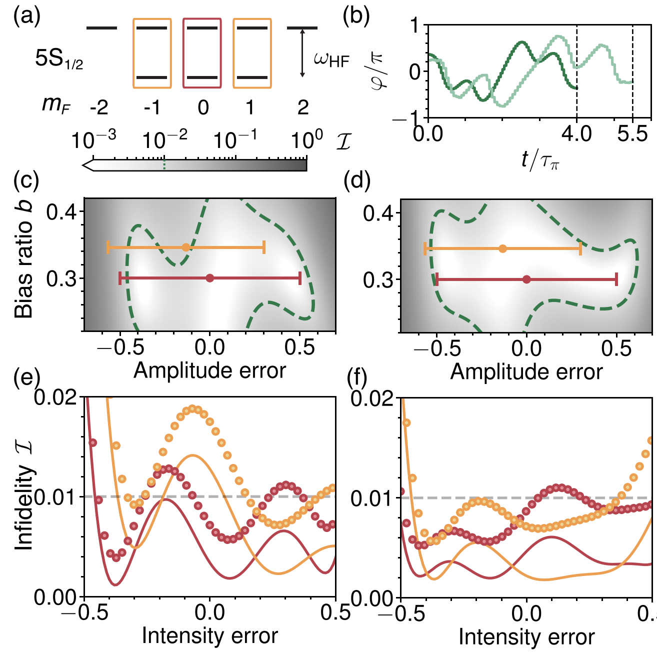

FIG. 3. CP-BR for $R_x(\pi)$ to address multiple hyperfine atomic spins. (a) The level diagram marks $\{|\uparrow_m\rangle, |\downarrow_m\rangle\}$ subspins defined on the ^{87}Rb ground-state hyperfine manifold. (b) The optimal phase profiles $\{\varphi_j\}_{\rm opt}$ with $\mathcal{A} = 4\pi$ [for (c) and (e)] and 5.5π [for (d) and (f)] [$N = 80$, before the $|\Omega_{\rm R}(t)|$ edge-smoothing, see Appendix A]. (c),(d) Performance of the ensemble optimized CP-BR in the parameter space $\mathcal{I}(\mathcal{A} + \varepsilon_\mathcal{A}, b)$ vs $(\varepsilon_\mathcal{A}/\mathcal{A}, b)$, with $\mathcal{A} = 4\pi, 5.5\pi$, respectively. The red and orange bars suggest the range of $(\varepsilon_\mathcal{A}/\mathcal{A}, b)$ for the ensemble control of $m = 0$ and ± 1 subspins, respectively. Dashed green lines label the 1% level. The corresponding color bar is shown on the top of (c). (e),(f) $\mathcal{I}$ vs ε_I/I for $m = 0$ (red) and $m = \pm 1$ (orange) subspins. The solid lines and circle symbols are from the two-level and full-model simulations, respectively. Among them, the optimization in (c) and (e) only averages $\varepsilon_\mathcal{A}$ along the red bar ($m = 0$ with $b = 0.3$) while the optimization in (d) and (f) averages $\{\varepsilon_\mathcal{A}, b\}$ combinations along both the red ($m = 0$ with $b = 0.3$) and orange ($m = \pm 1$ with $b = 0.35$) bars.

Here $\mathcal{F}^{(N)}(\mathcal{A} + \varepsilon_\mathcal{A}, b; \{\varphi_j\})$ is evaluated according to Eq. (4), but with $\tilde{U}$ replaced by $\tilde{U}^{(N)}(\mathcal{A} + \varepsilon_\mathcal{A}, b; \{\varphi_j\})$. In this work, benefitting from the simple $\tilde{U}(\mathcal{A}/N, b; \varphi_j)$ expression [Eq. (C4)], the GRAPE (gradient ascent pulse engineering) optimization (Appendix D) [49] is performed at the SU(2) level with Eq. (1) first. The optimal $\{\varphi_j\}_{\rm opt}$ are then transferred to the full model [Eq. (A1)] to validate the applicability of the CP-BR to real atoms.

An example of optimal $\overline{\mathcal{I}}_{\rm opt}(\mathcal{A}) = 1 - \overline{\mathcal{F}}_{\rm opt}(\mathcal{A})$ for $R_x(\pi)$ with improved amplitude-error resilience is shown in Fig. 2(a) versus pulse area number $m_\mathcal{A} = \mathcal{A}/\pi$ (circle symbols). Here, for the Eq. (7) optimization, the amplitude deviation uniformly samples $\varepsilon_\mathcal{A} \in (-0.5, 0.5)\mathcal{A}$. The bias ratio is set as $b = 0.0$ (MR, with $\Delta = 0.5\omega_{\rm HF}$) and $b = 0.3$ (BR, with $\Delta = 3.6\omega_{\rm HF}$). As in the Fig. 2(b) examples, we typically find $N/m_\mathcal{A} > 3$ to be enough for CP to reach the optimal performance. On the other hand, to help mitigating nonadiabatic $|e\rangle$ excitation, we set large enough $N = 80$ subpulses so that the optimal $\{\varphi_j\}_{\rm opt}$ can become quasicontinuous in time. The phase symmetry in Fig. 2(a,i-ii) is associated with the

x-rotation [50]. With Eq. (5), we include the minimal $\mathcal{I}_{\rm sp}$ into the SU(2) $\overline{\mathcal{I}}_{\rm opt}$, after straightforward light intensity average.

From Fig. 2(a) we observe increasingly efficient suppression of the average infidelity $\overline{\mathcal{I}}_{\rm opt}(\mathcal{A})$ with larger pulse area number $m_{\mathcal{A}}$, which is expected since redundant rotations on the Bloch sphere can be phased to improve the control robustness [17,20,51–53]. Interestingly, the enhancement to $\overline{\mathcal{I}}_{\rm opt}(\mathcal{A})$ with $\mathcal{A}$ displays stepwise features near certain integers $m_{\mathcal{A}}$, which are associated with an increased number of perfected $\mathcal{I}(\mathcal{A})$ within the $\pm 50\%$ $\varepsilon_{\mathcal{A}}/\mathcal{A}$ distribution, as shown by the Fig. 2(a)(i,ii) examples. The features could merit additional study in the future. Here, we note that increasing the average $\mathcal{A}$ leads to increased $I_{\rm sp}$ to limit the achievable $\overline{\mathcal{I}}_{\rm opt}$. For the particular ensemble control with the required error resilience, a balance is met at a suitable $\mathcal{A}_0$ for $\overline{\mathcal{I}}_{\rm opt}(\mathcal{A}_0)$ to reach its minimum. For the $\overline{\mathcal{I}}_{\rm opt}$ at the SU(2) level, we already see that the $R_x(\pi)$ gate in the BR regime performs substantially better when addressing the $\varepsilon_{\mathcal{A}}/\mathcal{A} = \pm 50\%$ amplitude distribution, with BR-$\overline{\mathcal{I}}_{\rm opt}(\mathcal{A}_0) \approx 0.5\%$ reached at $\mathcal{A}_0 \approx 5.5\pi$, as compared to MR-$\overline{\mathcal{I}}_{\rm opt}(\mathcal{A}_0) \approx 2\%$ at $\mathcal{A}_0 \approx 4\pi$, due to the better suppression of spontaneous emission.

In addition, we vary the amplitude-error range $\varepsilon_{\rm M}$ as $\varepsilon_{\mathcal{A}} \in (-\varepsilon_{\rm M}, \varepsilon_{\rm M})\mathcal{A}$ to study the performance of CP-BP optimized for various degrees of amplitude error resilience. As plotted in Fig. 2(c), the $\overline{\mathcal{I}}$ with $\mathcal{A} = 2.5\pi$ and 4π reaches their individual spontaneous-emission limits (points with zero amplitude error range) with $\varepsilon_{\rm M} = 0.15$ and 0.35, respectively. Clearly, if the control robustness can be compromised, such as in specific applications with a limited pulse-area broadening, then the CP-BR pulses with a smaller average pulse area can reach a better spontaneous-emission limited performance.

We now apply the SU(2)-optimized $\{\varphi_j\}_{\rm opt}$ to the full ^{87}Rb D1 model. As detailed in Appendix A, to mitigate nonadiabatic excitations to the $|e\rangle$ states during this step, $|\Omega_{\rm R}| \propto \sqrt{I_1 I_2}$ is edge-smoothed from a $\tau_c = m_{\mathcal{A}}\tau_\pi$ square pulse into a $\tau_c = (m_{\mathcal{A}}+1)\tau_\pi$ sine-shaped pulse (Appendix A), before the splitting into the N equal-area subpulses to associate with the quasicontinuous $\{\varphi_j\}_{\rm opt}$. Since $\delta \propto |\Omega_{\rm R}|$, the reshaped Raman pulse retains the full control advantages at the SU(2)-level by Eq. (1). In light of Fig. 1(e), we set the "π time" $\tau_\pi = 100\pi/\omega_{\rm HF}$ for the Fig. 2 simulation, with circle symbols to represent the associated BR-$\overline{\mathcal{I}}_{\rm opt}$ and MR-$\overline{\mathcal{I}}_{\rm opt}$.

In Fig. 2 we find that the BR-$\overline{\mathcal{I}}_{\rm opt}$ in the full model only degrades slightly from that by the two-level model. In contrast, the full model MR-$\overline{\mathcal{I}}_{\rm opt}$ (blue circle symbols) degrades substantially from the SU(2) prediction. Similar to Fig. 1(e), part of the degraded performance in both cases is associated with nonadiabatic $|e\rangle$ excitations. In addition, with the $\omega_{{\rm hfs},e} = 0.12\omega_{\rm HF}$ excited-state hyperfine splitting for ^{87}Rb [45] restored, the $\Delta m = \pm 2$ spin leakage [47] among the Zeeman sublevels is retained at a $\omega_{{\rm hfs},e}/\Delta$ level, during the $\Delta m = 0$ Raman excitation driven by linearly polarized pulses [Eq. (B2)] [30]. Due to the moderate $\Delta = 0.5\omega_{\rm HF}$, the spin leakages more severely affect MR-$\overline{\mathcal{I}}_{\rm opt}$. We note that within nanosecond τ_c, the spin-leakage among the Zeeman sublevels cannot be easily suppressed by the traditional bias-field method that sufficiently lifts the Zeeman degeneracy [31,54]. A CP-BR-compatible, large enough $\Delta \gg \omega_{{\rm hfs},e}$ is therefore important for isolating the target atomic spins [Figs. 3(a) and 4] during the fast spinor matterwave control.

Finally, we revisit the category of error sources that brings z-component variations to Raman Rabi vectors. First, we note that in both the BR and MR regime the detuning δ-error can be introduced by uncorrelated fluctuation of $I_{1,2}$ intensities. Such fluctuations are well-suppressed in the retroreflection geometry for Raman interferometry [31] where the Raman-$\mathbf{k}_{\rm R}$ direction is controlled, e.g., by optical delays [30,55]. Besides the Stark-shifted $\delta = b|\Omega_R|$, there are "bare" offsets $\delta_{\rm off}$ associated with Doppler and Zeeman shifts, as well as any time-dependent differential phase shifts to $\mathcal{E}_{1,2}$. These offset introduces error at the $\delta_{\rm off}\tau_c$ level. For example, for ^{87}Rb with $\tau_c \sim 100\pi/\omega_{\rm HF}$, we expect CP-BR to maintain $\mathcal{F} > 99\%$ in the presence of MHz-level $\delta_{\rm off}$ broadening (see Appendix F). This level of detuning tolerance is sufficient for typical cold atom and atomic beam experiments.

With the negligible $\delta_{\rm off}$, we consider CP-BR with a special kind of designed robustness—parallel control of multiple spin species with different bias ratios b [30]. This ability can potentially be useful for precision measurements [56] and quantum information processing [57,58]. As illustrated in Fig. 4 with the ^{87}Rb example, for a generic alkaline atom with $I > 1/2$ nuclear spin and when addressing $\{|\uparrow_m\rangle, |\downarrow_m\rangle\}$ pseudospins defined on the $F = I \pm 1/2$ hyperfine levels [Fig. 3(a)], with $m = m_F$, both the Raman Rabi frequency $\Omega_{{\rm R},m}$ and the bias ratio b_m become m-dependent [30,48]. We consider the linearly polarized composite pulse (Fig. 4) design to address all the $\{|\uparrow_m\rangle, |\downarrow_m\rangle\}$ subspins of ^{87}Rb. The optimization to achieve resilience against laser intensity error $\varepsilon_I/I \in (-0.5, 0.5)$ [Figs. 3(c) and 3(d)] is again performed at the SU(2) level first to obtain $\{\varphi_j\}_{\rm opt}$, which is then transferred to the full model. Figures 3(c) and 3(e) results are optimized for the $m = 0$ subspin only, covering $\varepsilon_{\mathcal{A}} \in (-0.5, 0.5)\mathcal{A}$ with $\mathcal{A} = 4\pi$ at $b = 0.3$. In contrast, Figs. 3(d) and 3(f) results are optimized to balance the performance for all the $m = 0, \pm 1$ subspins, covering $\varepsilon_{\mathcal{A}} \in (-0.5, 0.5)\mathcal{A}$ with $\mathcal{A} = 5.5\pi$ at $b = 0.3$ $(m = 0)$ and $\mathcal{A} = 4.7\pi$ at $b = 0.35$ $(m = \pm 1)$. The parameter coverages are marked with red $(m = 0)$ and orange $(|m| = 1)$ lines in the Figs. 3(c) and 3(d) parameter-space 2D plot of $\mathcal{I}$. The optimized phase $\{\varphi_j\}_{\rm opt}$ for the composite pulses is given in Fig. 3(b). The full model results in Figs. 3(e) and 3(f) are again with the pulse profile edge-smoothed at $\tau_\pi = 100\pi/\omega_{\rm HF}$, as those for Fig. 2 (Fig. 4). According to Fig. 3(f), we find $\overline{\mathcal{I}}_{\rm opt} \approx 9 \times 10^{-3}$ for the composite $R_x(\pi)$ gate when addressing all the ^{87}Rb subspins with the $\pm 50\%$ laser intensity distribution. This performance is only slightly compromised from the single $m = 0$ subspin result in Fig. 2(a), where $\overline{\mathcal{I}}_{\rm opt}(5.5\pi) \approx 7 \times 10^{-3}$ is reached. We numerically confirm that the fidelity is unaffected by polarization impurity of the Raman beams at the 1% level. The overall performance can be further improved with larger $\mathcal{A}$ by increasing Δ in proportion to maintain a low spontaneous-emission level.

IV. DISCUSSION AND OUTLOOK

Unlike microwave controls of quantum systems, which usually take place within a subwavelength volume with a uniform control intensity [42,44,59–62], optical controls are often far more prone to intensity inhomogeneities [63,64]. Nevertheless, high-fidelity control of macroscopic atomic samples is achievable by implementing NMR-inspired composite pulses [17–21], at properly chosen frequency ranges and timescales, where complications associated with multi-level excitation, spontaneous emission, and the atomic motion itself can be suppressed.

This work revisits spinor matterwave control techniques based on Raman excitations. Our work focuses in a regime of Raman control with $\Delta = O(\omega_{\rm HF})$ that supports high-speed operation with $\tau_c \sim 100\pi/\omega_{\rm HF}$ within nanoseconds, only limited by the ground-state hyperfine splitting. This choice of Δ leads to substantial light shift to the two-photon detuning δ. However, we have shown that taking advantage of perfect correlation between the δ and $\Omega_{\rm R}$ errors, composite biased rotations can be optimized for precise ensemble spinor matterwave control, even for multiple Zeeman pseudospins and when subjected to inhomogeneous laser illumination. We note that the ability to parallelly control multiple Zeeman pseudospins in neutral atoms can potentially be useful for cosensing of magnetic fields [56] during, e.g., inertial sensing and for ancillary steering of quantum information [57,58]. Related to the underlying geometric robustness [53,65], we find the optimal CP-BR to be fairly tolerant to the pulse parameter errors themselves, too (Appendix G). We also notice that beyond error suppression, CP-BR can be designed to enhance the parameter selectivity [21], such as for improving the spatial resolution when addressing arrays of samples [66].

So far, we have ignored the common Stark shift $\delta_{\rm com} = (\delta_\uparrow + \delta_\downarrow)/2$ to the spinor matterwave dynamics [31]. In the absence of spin-motion separation, i.e., with $|\psi_\downarrow(r)|^2 \propto |\psi_\uparrow(r)|^2$, then the common Stark shift does not affect the spinor coherence central to the interferometric measurements. However, after the spin-dependent momentum transfer, spin-motion separation develops necessarily in an interferometry sequence for sensing the spatial-dependent interactions, including those due to any spatially varying $\delta_{\rm com}$. A standard technique to counter the inhomogeneous $\delta_{\rm com}$ broadening relies on introducing additional sidebands to the $\mathcal{E}_{1,2}$ pulses with opposite Stark shifts [67], or, by taking advantage of nanosecond operations, to fire additional phase-trimming pulses in the time domain [30]. In the former case, the bias angle θ_b can be modified by the additional sidebands, which should be included during the CP-BR optimization.

Previously, high-speed spinor matterwave control at the nanosecond level was mostly considered for manipulating microscopically confined ions [7–9,12], typically involving THz-level single photon detuning Δ in the case of Raman excitation. By operating at tens of GHz detuning Δ, our proposal has the obvious advantage of reducing the laser intensity $I \propto \Delta$ requirement for the Raman control, thereby supporting rapid control of macroscopic samples even with milli-Watt level laser power [30]. More generally, the CP-BR method supports a suitable single-photon detuning Δ to balance the optical power efficiency with the requirements on the control speed and/or the suppression of excited-state dynamics. In addition to supporting the quantum-enhanced atom interferometry technology [13–16] for free-space samples, the CP-BR method can be particularly useful for tailoring repetitive, large-momentum-transfer-enhanced control of macroscopic samples moving at high speeds, such as for interferometric rotation sensing [2] and nanolithography [68] with lightly collimated, high-flux atomic beams. To this end, we anticipate further developments of wide-band pulse shaping techniques [69,70] for generating powerful, arbitrarily shapeable nanosecond pulses for spinor matterwave control of increasingly large atomic samples.

ACKNOWLEDGMENTS

We thank Jinming Cui, Yu Chen, Yizun He, and Jiangyong Hu for valuable discussions. We acknowledge support from National Key Research Program of China under Grant No. 2022YFA1404204, and from NSFC under Grant No. 12074083. H.Y. acknowledges partial support from the Research Grants Council of Hong Kong under Grants No. 14307420, No. 14308019, No. 14309022 and the hospitality of Shenzhen International Quantum Academy.

APPENDIX A: FULL NUMERICAL MODEL

The numerical simulation in this work is based on the full light-atom interaction Hamiltonian on the D1 line of ^{87}Rb, as schematically illustrated in Fig. 4, with the $5P_{1/2}$ hyperfine splitting $\omega_{{\rm hfs},e} = 2\pi \times 814.5$ MHz [45] adjusted to zero when necessary.

In Fig. 4, the Zeeman-degenerate hyperfine states are labeled as $|e_m\rangle, |\uparrow_m\rangle, |\downarrow_m\rangle$ with magnetic quantum number $m = m_F$, respectively. We consider counterpropagating laser pulses, $\mathbf{E}_{1,2} = \mathbf{e}_{1,2}\mathcal{E}_{1,2}e^{i(\mathbf{k}_{1,2}\cdot\mathbf{r}-\omega_{1,2}t)} + {\rm c.c.}$, with perpendicular linear $\mathbf{e}_{1,2}$ [30], shaped slowly varying amplitudes $\mathcal{E}_{1,2}(\mathbf{r}, t)$, and Raman-resonant carrier frequency difference $\omega_2 - \omega_1 = \omega_{\rm HF} = 2\pi \times 6.835$ GHz [45] to address the ground-state atom. Following the discussion in the main text, the effective,

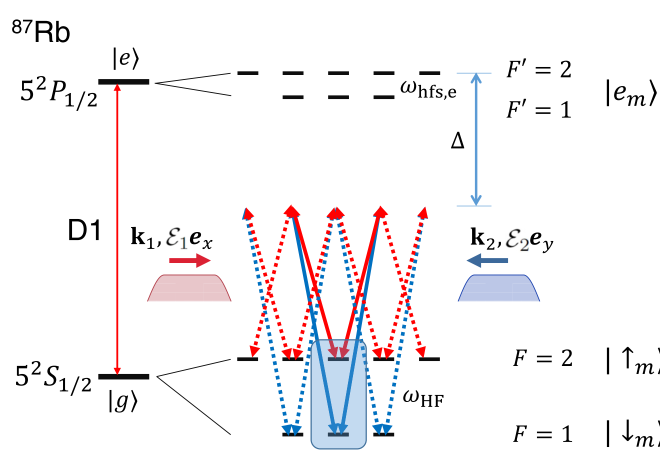

FIG. 4. Schematic diagram for the full ^{87}Rb D1 model. We consider counterpropagating $\mathbf{k}_{1,2}$ and linear $\perp$ linear polarization, with the quantization axis along $\mathbf{e}_z$ [30]. The "edge-smoothed" waveforms are highlighted. At $\Delta \gg \omega_{{\rm hfs},e}$, the hyperfine dynamics is decomposed into those within $\{|\uparrow_m\rangle, |\downarrow_m\rangle\}$ subspins ($m = -1, 0, 1$), with suppressed m-changing leakages [Eq. (B2)]. The $\{|\uparrow\rangle, |\downarrow\rangle\} = \{|\uparrow_0\rangle, |\downarrow_0\rangle\}$ subspin for Figs. 1(e), 1(f), and 2 is highlighted.

non-Hermitian Hamiltonian is

$$H_{\mathrm{eff}}(\mathbf{r},t)=\hbar\sum_{e,l}(\omega_e-\omega_{e0}-i\Gamma_e/2)\sigma^{e_le_l}+\hbar\sum_{c=\uparrow,\downarrow,m}(\omega_c-\omega_{g0})\sigma^{c_mc_m}+\frac{\hbar}{2}\sum_{c=\uparrow,\downarrow}\sum_{e,m,l}\Omega^j_{c_me_l}(\mathbf{r},t)\sigma^{c_me_l}+\mathrm{H.c.}\quad \text{(A1)}$$

Here ω_{e0},ω_{g0} are decided by the energy of the reference level in the excited- and ground-state manifolds, respectively, chosen as the top hyperfine levels in this work. The laser Rabi frequencies,

$$\Omega^j_{e_l\uparrow_m(\downarrow_n)}(\mathbf{r},t)\equiv-\frac{\langle e_l|\mathbf{d}\cdot\mathbf{e}_j\mathcal{E}_j(\mathbf{r},t)|\uparrow_m(\downarrow_n)\rangle}{\hbar},\quad \text{(A2)}$$

are accordingly written in the $\omega_{e0,g0}$ frame under the rotating-wave approximation. The $\mathbf{d}$ is the atomic electric dipole operator. The $\sigma^{\uparrow_me_l}=|\uparrow_m\rangle\langle e_l|$, $\sigma^{e_l\uparrow_m}=|e_l\rangle\langle\uparrow_m|$ are the raising and lowering operators between states $|\uparrow_m\rangle$ and $|e_l\rangle$. Similar σ operators are defined for all the other $|\uparrow_m\rangle$, $|\downarrow_n\rangle$, and $|e_l\rangle$ state combinations. In accordance with the discussions in the main text, Eq. (A1) can also be expressed as $H_{\mathrm{eff}}=H_0-i\hat{\Gamma}/2$, with $\hat{\Gamma}=\Gamma\sum_{e,l}\sigma^{e_le_l}$, $\Gamma=1/(27.7\,\mathrm{ns})$ to be the D1 linewidth [45].

Numerical evaluations of $\tilde{U}$ and the Eq. (4) gate fidelity $\mathcal{F}$ in the main text follow the Ref. [30] recipe based on the Eq. (A1) Hamiltonian here. In particular, the radiation damping is reflected in the decreasing norm of the wave function $|\psi\rangle$ [71]. During the gate fidelity evaluation, since any spontaneous emission is associated with complete decoherence, we only need to consider the non-Hermitian evolution without any quantum jump [72,73].

In the numerical simulations for Figs. 2 and 3 in the main text, we smooth the rising and falling edges of the area $\mathcal{A}$ square pulse. For that purpose, the pulse duration is first elongated from $\tau_c=m_{\mathcal{A}}\tau_\pi$ to $\tau_c=(m_{\mathcal{A}}+1)\tau_\pi$. Next, the first and last $\tau_\pi/2$ are reshaped to form the sine-shaped rising and falling edges (see Fig. 4), thereby slowly ramp up $|\Omega_{\mathrm{R}}|$ from zero to its maximum and back according to $\sin^2(t/\tau_\pi)$. Finally, the edge-smoothed pulse is divided into N equal-area parts to associate with the phase profile $\{\varphi_j\}$ of interest.

APPENDIX B: REDUCTION TO THE TWO-LEVEL MODEL

We refer readers to Ref. [30] for the reduction from Eq. (A1) to the Eq. (1) spinor Hamiltonian in the main text for the spinor $\{|\uparrow\rangle=|\uparrow_m\rangle,|\downarrow\rangle=|\downarrow_m\rangle\}$ defined on a pair of hyperfine Zeeman sublevels (Fig. 4). Here we generally note that with a slight rotation of the H_0 basis and by expressing (after a hyperfine rotating wave transformation)

$$H_{\mathrm{eff}}=H+V'-i\hat{\Gamma}/2,\quad \text{(B1)}$$

then the V' term includes all the unitary corrections from the full model, including the m-sensitive light shifts and couplings. For the linearly polarized $\mathbf{e}_{1,2}$ that only drives the $\Delta m=\pm2$ leakages among Zeeman sublevels [47], the leakages are associated with a coupling strength:

$$\Omega^{\pm2}=O\left(\frac{\omega_{\mathrm{hfs,e}}}{\Delta}\right)\Omega_{\mathrm{R}}.\quad \text{(B2)}$$

Therefore, increasing Δ suppresses the spin leakage. Other terms in V' corrections are at least $1/\Delta^2$-suppressed too, except for the (m-insensitive) δ_{com} common shift as discussed in Sec. IV. In the large Δ limit so that the V' contribution to atomic state dynamics vanishes, the decay loss by $\hat{\Gamma}$ is decided by the linewidth of the instantaneous "dressed" ground states, as discussed in the main text with Eq. (5).

APPENDIX C: BIASED ROTATION

Following Eq. (A1), we consider a spinor $|\{|\uparrow\rangle=|\uparrow_m\rangle,|\downarrow\rangle=|\downarrow_m\rangle\}$ defined on a pair of ground-state hyperfine Zeeman-sublevels. As depicted in Fig. 1(a), resonant Raman coupling is induced by $\Omega_{1,2}$ to coherently couple $|\uparrow\rangle$ and $|\downarrow\rangle$, forming an effective spin-1/2 system subjected to the Eq. (1) Hamiltonian. The two-photon shift by Eq. (2) is $\delta=\delta_\uparrow-\delta_\downarrow$ with

$$\delta_\uparrow=\frac{|\Omega_1|^2}{4\Delta}+\frac{|\Omega_2'|^2}{4(\Delta+\omega_{\mathrm{HF}})},\qquad \delta_\downarrow=\frac{|\Omega_2|^2}{4\Delta}+\frac{|\Omega_1'|^2}{4(\Delta-\omega_{\mathrm{HF}})}.\quad \text{(C1)}$$

Notice while $\Omega_{1,2},\Omega'_{1,2}\propto\sqrt{I_{1,2}}$, the relative strengths between $\Omega_{1,2}$ and $\Omega'_{1,2}$ are determined by the associated dipole transition matrix elements. Here, we consider the example of $I_1=I_2$ when driving the spinor defined on the D1 line so that $|\Omega_{1,2}|=|\Omega'_{1,2}|=\Omega$. In this case,

$$\delta=\delta_\uparrow-\delta_\downarrow=\frac{|\Omega|^2}{4(\Delta+\omega_{\mathrm{HF}})}-\frac{|\Omega|^2}{4(\Delta-\omega_{\mathrm{HF}})}=-\frac{|\Omega|^2\omega_{\mathrm{HF}}}{2(\Delta+\omega_{\mathrm{HF}})(\Delta-\omega_{\mathrm{HF}})},\quad \text{(C2)}$$

with a bias ratio

$$b=\tan\theta_b=\frac{\delta}{\Omega_R}=-\frac{\Delta\omega_{\mathrm{HF}}}{(\Delta-\omega_{\mathrm{HF}})(\Delta+\omega_{\mathrm{HF}})}.\quad \text{(C3)}$$

At an arbitrary pulse area $\mathcal{A}$, the SU(2) evolution is described by a propagator

$$U(\mathcal{A},b,\varphi)=\mathbf{1}\cos\frac{\tilde{\phi}}{2}-i\sin\frac{\tilde{\phi}}{2}\frac{\sigma_x\cos\varphi+\sigma_y\sin\varphi+b\sigma_z}{\sqrt{1+b^2}}\quad \text{(C4)}$$

with rotation angle $\tilde{\phi}=\sqrt{1+b^2}\mathcal{A}$. As illustrated in Fig. 1(b) in the main text, due to the finite b, the available rotating axes n are biased from the equator by a fixed angle θ_b, for which we refer to the associated SU(2) controls as "biased rotation" (BR).

APPENDIX D: GRAPE OPTIMIZATION

We use a gradient-based optimization algorithm called GRAPE (gradient ascent pulse engineering) [49] to optimize the target gates. Specifically, for each phases φ_i at each iteration, its gradient is

$$g_i = -\frac{\partial \mathcal{F}}{\partial \tilde{U}} \frac{\partial \tilde{U}}{\partial \varphi_i}. \tag{D1}$$

The $\partial \mathcal{F}/\partial \tilde{U}$ is obtained from Eq. (4) directly, while the second term is

$$\frac{\partial \tilde{U}}{\partial \varphi_i} = \tilde{U}_N \cdots \tilde{U}_{i+1} \frac{\partial \tilde{U}_i}{\partial \varphi_i} \tilde{U}_{i-1} \cdots \tilde{U}_1. \tag{D2}$$

The $\tilde{U}_j'$s are evaluated by Eq. (C4). We further have

$$\frac{\partial \tilde{U}}{\partial \varphi} = -i \sin \frac{\tilde{\phi}}{2} \frac{\sigma_y \cos \varphi - \sigma_x \sin \varphi}{\sqrt{1+b^2}}. \tag{D3}$$

During the optimization for the $\mathcal{A}$-error resilience, the gradients are averaged over a list of errors $\{\varepsilon_{\mathcal{A}}\}$,

$$\overline{g_i}(\mathcal{A}, b; \{\varphi_j\}) = \langle g(\mathcal{A} + \varepsilon_{\mathcal{A}}, b; \{\varphi_j\}) \rangle_{\{\varepsilon_{\mathcal{A}}\}}. \tag{D4}$$

The analytical evaluation of the propagators and gradients at SU(2) level helps to improve the computational efficiency and precision for the GRAPE optimization.

APPENDIX E: $\pi/2$ GATE

Our discussions of CP-BR in the main text exploit the $R_x(\pi)$ example. In this Appendix, we present an additional example of $R_x(\pi/2)$ with amplitude-error resilience. The results are presented in Fig. 5. Similar to the $R_x(\pi)$ case, the amplitude deviation uniformly samples $\varepsilon_{\mathcal{A}} \in (-0.5, 0.5)\mathcal{A}$. The bias ratio is again set as $b = 0.0$ (MR, with $\Delta = 0.5\omega_{\rm HF}$) and $b = 0.3$ (BR, with $\Delta = 3.6\omega_{\rm HF}$). The $\overline{\mathcal{I}}_{\rm opt}(\mathcal{A})$ versus $\mathcal{A}$ for the case of CP-BR (green line and symbols) shows stepwise features, similar to the $R_x(\pi)$ case in Fig. 2. Comparing to the $R_x(\pi)$ results, here the "plateau" pulse area $\mathcal{A}$ following significant improvements to $R_x(\pi/2)$ ($m_{\mathcal{A}} = 2$ and 3.5 in Fig. 5) is approximately $\pi/2$ less, which is somewhat expected as the desired $\pi/2$ rotating angle of $R_x(\pi/2)$ is $\pi/2$ less than that for $R_x(\pi)$. Similar to the $R_x(\pi)$ results in Fig. 2(a), the performance of the full-model $\overline{\mathcal{I}}$ degrades more substantially for the MR case, due to the more severe spin-leakage as discussed in the main text. The apparently more severe BR-$\overline{\mathcal{I}}$ degradation is actually due to the improved fidelity for the $R_x(\pi/2)$ at the SU(2) level here (green circle symbols), compared to the $R_x(\pi)$ case, which makes the difference more apparent.

APPENDIX F: ROBUSTNESS TO BARE TWO-PHOTON DETUNING ERROR

In the main text, we clarified that errors induced by bare two-photon detuning $\delta_{\rm off}$, such as those associated with Doppler and Zeeman shifts, become negligible when $\delta_{\rm off}\tau_c \ll 1$ during the nanosecond control. In this Appendix, we use the Fig. 2(i) example to quantify this statement. As shown in Fig. 6, without any tailored optimization, the CP-BR solutions are naturally immune to $\delta_{\rm off}$ at the 99% level within the $\delta_{\rm off}/\Omega_R \sim \pm 0.05$ range. Using ^{87}Rb with $\tau_\pi = 100\pi/\omega_{\rm HF}$ as an example, the robustness range of $\delta_{\rm off}$ is around $2\pi \times 7$ MHz, which covers well the Doppler and Zeeman shifts in typical interferometric experiments. Since the CP-BR is optimized on the δ-$|\Omega_{\rm R}|$ plane along a line with "tilted" angle θ_b, CP-BR naturally have a certain level of immunity to $\delta_{\rm off}$ along the δ-axis. Further enhanced $\delta_{\rm off}$-tolerance can be achieved by tailored optimization of $\mathcal{F}$ at the expense of either reduced $\overline{\mathcal{F}}$ or increased pulse area requirements.

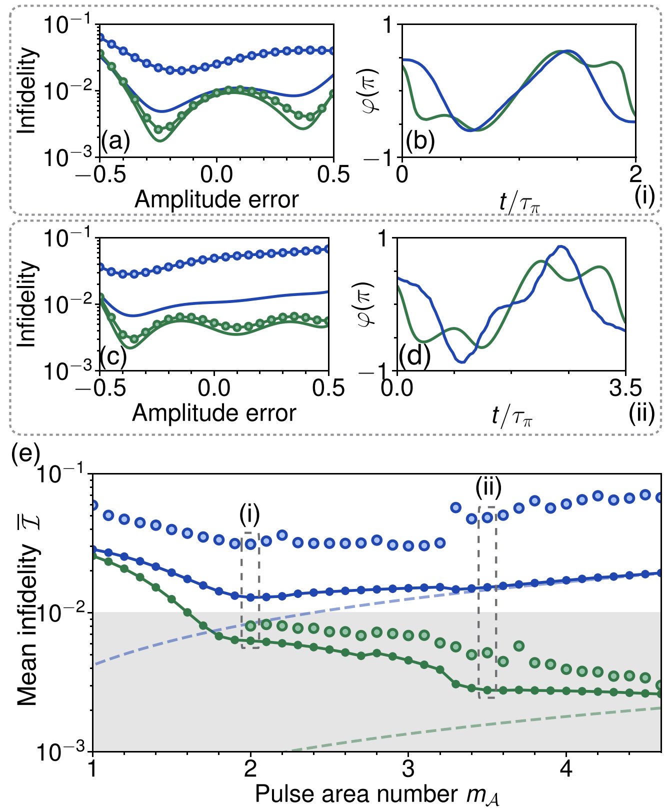

FIG. 5. CP-BR for $R_x(\pi/2)$. Parts (a),(b) correspond to Fig. 2(a)(i) in the main text, but with $\mathcal{A} = 2\pi$. Parts (c),(d) correspond to Fig. 2(a)(ii) in the main text, but with $\mathcal{A} = 3.5\pi$. These pulse areas are highlighted in (e) near the plateaus after the stepwise improvements to $\overline{\mathcal{I}}$ occur.

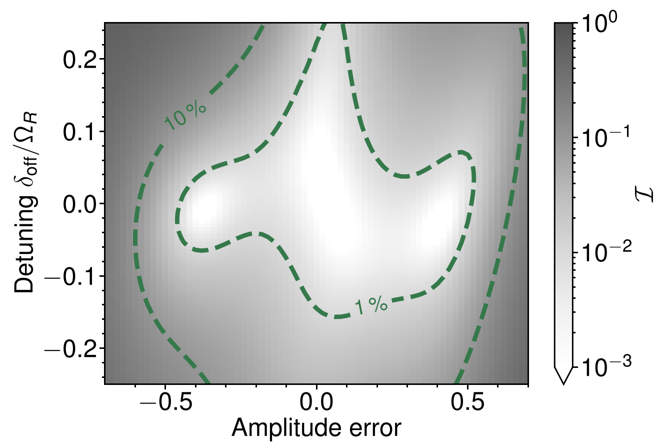

FIG. 6. Infidelities $\mathcal{I}$ of CP-BR for $R_x(\pi)$ against bare two-photon detuning and amplitude errors. Here we choose the CP pulse with bias ratio $b = 0.3$ and $\mathcal{A} = 4\pi$, as in Fig. 2(i).

APPENDIX G: NONPERFECT IMPLEMENTATION

In Fig. 2 in the main text and Fig. 5, here we have shown that CP-BR achieves high-fidelity control ($\overline{\mathcal{F}} > 99\%$) in the presence of $\varepsilon_{\mathcal{A}} \in (-0.5, 0.5)\mathcal{A}$ amplitude errors. However, in real experiments, one can never implement CP with perfect amplitudes and phases as desired. To test the robustness of our CP solutions against nonperfect implementations, we consider the $R_x(\pi)$ example in Fig. 2 for a case study by evaluating the CP-BR performance in the presence of random noise among the subpulses. For each test, the random amplitude deviations uniformly sample between $\pm\sigma$, so that the relative amplitude of each subpulse is between $\tilde{C}_i = (1 \pm \sigma)C_i$. The average $\overline{\mathcal{I}}$ from 100 random tests is plotted against the maximum noise level σ in Fig. 7(a) with solid lines, while still covering the $\varepsilon_{\mathcal{A}} \in (-0.5, 0.5)\mathcal{A}$ mean amplitude error. The shadings suggest the 90% variance from these 100 tests. The red, blue, and green lines correspond to pulse areas and pulse number as $(m_{\mathcal{A}}, N) = (4, 20), (4, 80), (5.5, 80)$, respectively. For $m_{\mathcal{A}} = 4$ and $N = 20$, the nonperfect CP implementation starts to impact the control fidelities when the noise level is larger than 5%. From Fig. 7 we also see that a larger pulse number N supports a stronger tolerance to waveform imperfections. For the $m_{\mathcal{A}} = 4$ and $N = 80$ cases, the maximally allowed deviations can be as large as 10% while maintaining target fidelity. On the other hand, for large pulse area $\mathcal{A}$ so that the actual pulse area per subpulse increases, the maximally allowed random noise level decreases. The case of random phase noise is similar to the case of amplitude, as in Fig. 7(b). Practically, we note that accurate waveforms with a precision better than 95% can be programed directly with a wide-band optical waveform generation technique developed recently [69,70] after moderate waveform calibration.

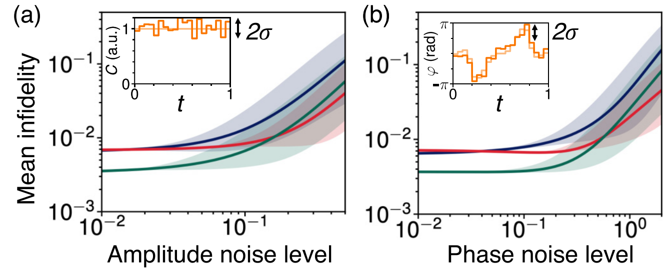

FIG. 7. Performance of CP-BR for $R_x(\pi)$ with $b = 0.3$, with random amplitude and phase noises distributed among the N subpulses. The red, blue, and green lines denote $(m_{\mathcal{A}}, N) = (4, 20), (4, 80), (5.5, 80)$, respectively. (a) $\overline{\mathcal{I}}$ as those in Fig. 2(a) perturbed by random amplitude noise vs the noise level. (b) $\overline{\mathcal{I}}$ as those in Fig. 2(a) perturbed by random phase noise vs the noise level.

[1] A. Peters, K. Y. Chung, B. Young, J. Hensley, and S. Chu, Precision atom interferometry, Philos. Trans. R. Soc. London A **355**, 2223 (1997).

[2] T. L. Gustavson, A. Landragin, and M. A. Kasevich, Rotation sensing with a dual atom-interferometer Sagnac gyroscope, Class. Quantum Grav. **17**, 2385 (2000).

[3] Z.-K. Hu, B.-L. Sun, X.-C. Duan, M.-K. Zhou, L.-L. Chen, S. Zhan, Q.-Z. Zhang, and J. Luo, Demonstration of an ultrahigh-sensitivity atom-interferometry absolute gravimeter, Phys. Rev. A **88**, 043610 (2013).

[4] C. Overstreet, P. Asenbaum, J. Curti, M. Kim, and M. A. Kasevich, Observation of a gravitational Aharonov-Bohm effect, Science **375**, 226 (2022).

[5] C. Gross and I. Bloch, Quantum simulations with ultracold atoms in optical lattices, Science **357**, 995 (2017).

[6] A. J. Daley, I. Bloch, C. Kokail, S. Flannigan, N. Pearson, M. Troyer, and P. Zoller, Practical quantum advantage in quantum simulation, Nature (London) **607**, 667 (2022).

[7] J. J. García-Ripoll, P. Zoller, and J. I. Cirac, Speed optimized two-qubit gates with laser coherent control techniques for ion trap quantum computing, Phys. Rev. Lett. **91**, 157901 (2003).

[8] L. M. Duan, Scaling ion trap quantum computation through fast quantum gates, Phys. Rev. Lett. **93**, 100502 (2004).

[9] J. Mizrahi, C. Senko, B. Neyenhuis, K. G. Johnson, W. C. Campbell, C. W. S. Conover, and C. Monroe, Ultrafast spin-motion entanglement and interferometry with a single atom, Phys. Rev. Lett. **110**, 203001 (2013).

[10] H. Y. Lo, D. Kienzler, L. De Clercq, M. Marinelli, V. Negnevitsky, B. C. Keitch, and J. P. Home, Spin-motion entanglement and state diagnosis with squeezed oscillator wavepackets, Nature (London) **521**, 336 (2015).

[11] C. Flühmann, T. L. Nguyen, M. Marinelli, V. Negnevitsky, K. Mehta, and J. P. Home, Encoding a qubit in a trapped-ion mechanical oscillator, Nature (London) **566**, 513 (2019).

[12] D. Heinrich, M. Guggemos, M. Guevara-Bertsch, M. I. Hussain, C. F. Roos, and R. Blatt, Ultrafast coherent excitation of a 40Ca+ ion, New J. Phys. **21**, 073017 (2019).

[13] S. S. Szigeti, S. P. Nolan, J. D. Close, and S. A. Haine, High precision, quantum-enhanced gravimetry with a bose-einstein condensate, Phys. Rev. Lett. **125**, 100402 (2020).

[14] Y. Wu, R. Krishnakumar, J. Martínez-Rincón, B. K. Malia, O. Hosten, and M. A. Kasevich, Retrieval of cavity-generated atomic spin squeezing after free-space release, Phys. Rev. A **102**, 012224 (2020).

[15] G. P. Greve, C. Luo, B. Wu, and J. K. Thompson, Entanglement-enhanced matter-wave interferometry in a high-finesse cavity, Nature (London) **610**, 472 (2022).

[16] F. Anders, A. Idel, P. Feldmann, D. Bondarenko, S. Loriani, K. Lange, J. Peise, M. Gersemann, B. Meyer-Hoppe, S. Abend, N. Gaaloul, C. Schubert, D. Schlippert, L. Santos, E. Rasel, and C. Klempt, Momentum entanglement for atom interferometry, Phys. Rev. Lett. **127**, 140402 (2021).

[17] M. H. Levitt, Composite pulses, Prog. Nucl. Magn. Reson. Spectrosc. **18**, 61 (1986).

[18] T. E. Skinner, T. O. Reiss, B. Luy, N. Khaneja, and S. J. Glaser, Application of optimal control theory to the design of broadband excitation pulses for high-resolution NMR, J. Magn. Reson. **163**, 8 (2003).

[19] J. Ruths and J. S. Li, Optimal control of inhomogeneous ensembles, IEEE Trans. Autom. Contr. **57**, 2021 (2012).
[20] J. S. Li and N. Khaneja, Control of inhomogeneous quantum ensembles, Phys. Rev. A **73**, 030302(R) (2006).
[21] G. H. Low, T. J. Yoder, and I. L. Chuang, Methodology of resonant equiangular composite quantum gates, Phys. Rev. X **6**, 041067 (2016).
[22] J. M. McGuirk, M. J. Snadden, and M. A. Kasevich, Large area light-pulse atom interferometry, Phys. Rev. Lett. **85**, 4498 (2000).
[23] H. Müller, S. W. Chiow, S. Herrmann, and S. Chu, Atom interferometers with scalable enclosed area, Phys. Rev. Lett. **102**, 240403 (2009).
[24] K. Kotru, D. L. Butts, J. M. Kinast, and R. E. Stoner, Large-area atom interferometry with frequency-swept raman adiabatic passage, Phys. Rev. Lett. **115**, 103001 (2015).
[25] M. Jaffe, V. Xu, P. Haslinger, H. Müller, and P. Hamilton, Efficient adiabatic spin-dependent kicks in an atom interferometer, Phys. Rev. Lett. **121**, 040402 (2018).
[26] J. Mizrahi, B. Neyenhuis, K. G. Johnson, W. C. Campbell, C. Senko, D. Hayes, and C. Monroe, Quantum control of qubits and atomic motion using ultrafast laser pulses, Appl. Phys. B **114**, 45 (2014).
[27] M. Kasevich and S. Chu, Atomic interferometry using stimulated raman transitions, Phys. Rev. Lett. **67**, 181 (1991).
[28] P. Berg, S. Abend, G. Tackmann, C. Schubert, E. Giese, W. P. Schleich, F. A. Narducci, W. Ertmer, and E. M. Rasel, Composite-light-pulse technique for high-precision atom interferometry, Phys. Rev. Lett. **114**, 063002 (2015).
[29] J. Saywell, M. Carey, M. Belal, I. Kuprov, and T. Freegarde, Optimal control of Raman pulse sequences for atom interferometry, J. Phys. B **53**, 085006 (2020).
[30] L. Qiu, L. Ji, J. Hu, Y. He, Y. Wang, and S. Wu, Spinor matter-wave control with nanosecond spin-dependent kicks, PRX Quantum **3**, 040301 (2022).
[31] D. S. Weiss, B. C. Young, and S. Chu, Precision measurement of $\hbar$/mCs based on photon recoil using laser-cooled atoms and atomic interferometry, Appl. Phys. B **59**, 217 (1994).
[32] M. O. Scully and M. S. Zubairy, *Quantum Optics* (Cambridge University Press, Cambridge, 1997).
[33] J. Rudolph, T. Wilkason, M. Nantel, H. Swan, C. M. Holland, Y. Jiang, B. E. Garber, S. P. Carman, and J. M. Hogan, Large momentum transfer clock atom interferometry on the 689 nm intercombination line of strontium, Phys. Rev. Lett. **124**, 083604 (2020).
[34] T. Wilkason, M. Nantel, J. Rudolph, Y. Jiang, B. E. Garber, H. Swan, S. P. Carman, M. Abe, and J. M. Hogan, Atom interferometry with floquet atom optics, Phys. Rev. Lett. **129**, 183202 (2022).
[35] D. J. Wineland, M. Barrett, J. Britton, J. Chiaverini, B. DeMarco, W. M. Itano, B. Jelenkovic, C. Langer, D. Leibfried, V. Meyer, T. Rosenband, and T. Schatz, Quantum information processing with trapped ions, Philos. Trans. R. Soc. London A **361**, 1349 (2003).
[36] S. Wu, Y.-J. Wang, Q. Diot, and M. Prentiss, Splitting matter waves using an optimized standing-wave light-pulse sequence, Phys. Rev. A **71**, 043602 (2005).
[37] K. J. Hughes, B. Deissler, J. H. T. Burke, and C. A. Sackett, High-fidelity manipulation of a Bose-Einstein condensate using an optical standing wave, Phys. Rev. A **76**, 035601 (2007).
[38] C. D. Herold, V. D. Vaidya, X. Li, S. L. Rolston, J. V. Porto, and M. S. Safronava, Precision measurement of transition matrix elements via light shift cancellation, Phys. Rev. Lett. **109**, 243003 (2012).
[39] K. D. Nelson, C. D. Fertig, P. Hamilton, J. M. Brown, B. Estey, H. Müller, and R. L. Compton, Guided matter wave inertial sensing in a miniature physics package, Appl. Phys. Lett. **116**, 234002 (2020).
[40] More specifically, with $\mathbf{k}_{\rm eff}\cdot\mathbf{v}\tau_c \ll 1$ for all the matterwave velocity components of interest.
[41] Practically, the uniform intensity requirement can be reasonably well satisfied for atomic samples with size $\sigma \ll w$ within the Rayleigh range of the $\mathcal{E}_{1,2}$ Gaussian profile with $w \gg \lambda$.
[42] T. P. Harty, D. T. C. Allcock, C. J. Ballance, L. Guidoni, H. A. Janacek, N. M. Linke, D. N. Stacey, and D. M. Lucas, High-fidelity preparation, gates, memory, and readout of a trapped-ion quantum bit, Phys. Rev. Lett. **113**, 220501 (2014).
[43] C. J. Ballance, T. P. Harty, N. M. Linke, M. A. Sepiol, and D. M. Lucas, High-fidelity quantum logic gates using trapped-ion hyperfine qubits, Phys. Rev. Lett. **117**, 060504 (2016).
[44] Y. Wang, A. Kumar, T.-Y. Wu, and D. S. Weiss, Single-qubit gates based on targeted phase shifts in a 3D neutral atom array, Science **352**, 1562 (2016).
[45] D. A. Steck, Rubidium 87 D Line Data, available online at http://steck.us/alkalidata (revision 2.3.2, 10 September 2023).
[46] E. Magesan, J. M. Gambetta, and J. Emerson, Characterizing quantum gates via randomized benchmarking, Phys. Rev. A **85**, 042311 (2012).
[47] W. Happer, Optical pumping, Rev. Mod. Phys. **44**, 169 (1972).
[48] A. Dunning, R. Gregory, J. Bateman, N. Cooper, M. Himsworth, J. A. Jones, and T. Freegarde, Composite pulses for interferometry in a thermal cold atom cloud, Phys. Rev. A **90**, 033608 (2014).
[49] N. Khaneja, T. Reiss, C. Kehlet, T. Schulte-Herbrüggen, and S. J. Glaser, Optimal control of coupled spin dynamics: Design of NMR pulse sequences by gradient ascent algorithms, J. Magn. Reson. **172**, 296 (2005).
[50] K. Kobzar, S. Ehni, T. E. Skinner, S. J. Glaser, and B. Luy, Exploring the limits of broadband 90° and 180° universal rotation pulses, J. Magn. Reson. **225**, 142 (2012).
[51] S. L. Zhu and Z. D. Wang, Implementation of universal quantum gates based on nonadiabatic geometric phases, Phys. Rev. Lett. **89**, 097902 (2002).
[52] T. Ichikawa, M. Bando, Y. Kondo, and M. Nakahara, Geometric aspects of composite pulses, Philos. Trans. R. Soc. A **370**, 4671 (2012).
[53] E. Barnes, X. Wang, and S. Das Sarma, Robust quantum control using smooth pulses and topological winding, Sci. Rep. **5**, 12685 (2015).
[54] M. Kasevich and S. Chu, Measurement of the gravitational acceleration of an atom with a light-pulse atom interferometer, Appl. Phys. B **54**, 321 (1992).
[55] I. Perrin, J. Bernard, Y. Bidel, A. Bonnin, N. Zahzam, C. Blanchard, A. Bresson, and M. Cadoret, Zero-velocity atom interferometry using a retroreflected frequency-chirped laser, Phys. Rev. A **100**, 053618 (2019).
[56] C. L. Degen, F. Reinhard, and P. Cappellaro, Quantum sensing, Rev. Mod. Phys. **89**, 035002 (2017).
[57] W. L. Ma, M. Zhang, Y. Wong, K. Noh, S. Rosenblum, P. Reinhold, R. J. Schoelkopf, and L. Jiang, Path-independent

quantum gates with noisy ancilla, Phys. Rev. Lett. **125**, 110503 (2020).

[58] V. V. Albert, J. P. Covey, and J. Preskill, Robust encoding of a qubit in a molecule, Phys. Rev. X **10**, 031050 (2020).

[59] X. Rong, J. Geng, F. Shi, Y. Liu, K. Xu, W. Ma, F. Kong, Z. Jiang, Y. Wu, and J. Du, Experimental fault-tolerant universal quantum gates with solid-state spins under ambient conditions, Nat. Commun. **6**, 8748 (2015).

[60] P. R. Zangara and H. M. Pastawski, Loschmidt echo in many-spin systems: A quest for intrinsic decoherence and emergent irreversibility, Phys. Scr. **92**, 033001 (2017).

[61] J. Li, R. Fan, H. Wang, B. Ye, B. Zeng, H. Zhai, X. Peng, and J. Du, Measuring out-of-time-order correlators on a nuclear magnetic resonance quantum simulator, Phys. Rev. X **7**, 031011 (2017).

[62] G. A. Starkov and B. V. Fine, Free induction decays in nuclear spin- 2 lattices with a small number of interacting neighbors: The cases of silicon and fluorapatite, Phys. Rev. B **101**, 024428 (2020).

[63] C. Brif, R. Chakrabarti, and H. Rabitz, Control of quantum phenomena: past, present and future, New J. Phys. **12**, 075008 (2010).

[64] C. P. Koch, M. Lemeshko, and D. Sugny, Quantum control of molecular rotation, Rev. Mod. Phys. **91**, 035005 (2019).

[65] C. Kabytayev, T. J. Green, K. Khodjasteh, M. J. Biercuk, L. Viola, and K. R. Brown, Robustness of composite pulses to time-dependent control noise, Phys. Rev. A **90**, 012316 (2014).

[66] D. Bluvstein, H. Levine, G. Semeghini, T. T. Wang, S. Ebadi, M. Kalinowski, A. Keesling, N. Maskara, H. Pichler, M. Greiner, V. Vuletić, and M. D. Lukin, A quantum processor based on coherent transport of entangled atom arrays, Nature (London) **604**, 451 (2022).

[67] P. Asenbaum, C. Overstreet, M. Kim, J. Curti, and M. A. Kasevich, Atom-interferometric test of the equivalence principle at the 10-12 level, Phys. Rev. Lett. **125**, 191101 (2020).

[68] K. S. Johnson, J. H. Thywissen, N. H. Dekker, K. K. Berggren, A. P. Chu, R. Younkin, and M. Prentiss, Localization of metastable atom beams with optical standing waves: Nanolithography at the heisenberg limit, Science **280**, 1583 (1998).

[69] Y. He, L. Ji, Y. Wang, L. Qiu, J. Zhao, Y. Ma, X. Huang, S. Wu, and D. E. Chang, Geometric control of collective spontaneous emission, Phys. Rev. Lett. **125**, 213602 (2020).

[70] Y. Wang, Y. He, L. Ji, J. Hu, X. Huang, Y. Ma, L. Qiu, K. Zhao, and S. Wu, Intense, wideband optical waveform generation by self-balanced amplification of fiber electro-optical sideband modulation, Chin. Opt. Lett. **20**, 111401 (2022).

[71] R. Dum, A. S. Parkins, P. Zoller, and C. W. Gardiner, Monte Carlo simulation of master equations in quantum optics for vacuum, thermal, and squeezed reservoirs, Phys. Rev. A **46**, 4382 (1992).

[72] J. Dalibard, Y. Castin, and K. Molmer, Wave-function approach to dissipative processes in quantum optics, Phys. Rev. Lett. **68**, 580 (1992).

[73] H. J. Carmichael, *An Open Systems Approach to Quantum Optics*, Lecture Notes in Physics: Monographs, Vol. 18 (Springer, Berlin, 1993).